RESEARCH ARTICLE

Quantifying the influence of atmospheric rivers on rainfall over the Jianghuai River Basin during the 2022 Mei-yu season

Y. Zhang[1] | Y. Han[1] | Y. Xuan[2] | H. Zhou[3] | H. Gao[4] | N. Yang[1]

[1]Key Laboratory of Hydrometeorological Disaster Mechanism and Warning of Ministry of Water Resources, Nanjing University of Information Science and Technology, Nanjing, China

[2]Department of Civil Engineering, Faculty of Science and Engineering, Swansea University Bay Campus, Swansea, UK

[3]Anhui Key Laboratory of Atmospheric Science and Satellite Remote Sensing, Anhui Institute of Meteorology Sciences, Hefei, China

[4]School of Atmospheric Physics, Nanjing University of Information Science and Technology, Nanjing, China

Correspondence
H. Zhou, Anhui Institute of Meteorology Sciences, Anhui Key Laboratory of Atmospheric Science and Satellite Remote Sensing, Hefei, 230031, China.
Email: zhf_ahqx@163.com

Abstract

Atmospheric rivers (ARs) are narrow, elongated belts of intense water vapor transport that often occur in mid-latitude areas and are the primary drivers of heavy precipitation in these regions. This study investigates the impact of ARs on precipitation patterns in the Jianghuai River Basin during the Mei-yu period. Focusing on a specific rainstorm event on June 27, 2022, we analyze atmospheric circulation, water vapor attributes, and transport trajectories. Three distinct classes of grids (Class A, significantly influenced by ARs; Class B, moderately affected; and Class C, untouched by ARs) are identified based on their response to ARs. Class A grids, located centrally, experience substantial precipitation, with a higher probability of rainstorm events. Class B grids, situated at a distance from ARs, exhibit moderate precipitation and a longer duration of rainy days. Class C grids, minimally affected by ARs, experience minimal precipitation with almost no chance of rainstorm events. The results from grid-based analysis emphasize the localized influence of ARs, indicating a 8–30 times increase in precipitation intensity of Class A compared to Class C. The 23-day Mei-yu period is further categorized into AR days and non-AR days, revealing that ARs amplify precipitation intensity by 2–5 times on average. Grid-based and day-based analyses provide complementary insights, with the former offering a broader spatial perspective and the latter emphasizing temporal distinctions. These findings underscore the nuanced influence of ARs on precipitation, emphasizing their role in extreme events and highlighting the importance of considering both spatial and temporal factors in understanding precipitation variability.

KEYWORDS

amplifying effect, atmospheric rivers, Mei-yu season, precipitation patterns

1 | INTRODUCTION

Precipitation plays a critical role in Earth's water and energy cycles and stands as a pivotal factor in the Earth's climate system (Limsakul & Singhruck, 2016). Among all meteorological variables, changes in precipitation often have a significant impact on both human society and the natural environment, making it perhaps the most directly consequential facet affecting human life and civilization

(Gao *et al.*, 2018). In recent decades, particularly against the backdrop of global warming, the frequency and intensity of rainstorm events have escalated worldwide (Wang *et al.*, 2023). Furthermore, the resulting disasters, such as floods, debris flows, and landslides induced by rainstorms, as well as severe convective weather phenomena like lightning and hail often accompanying these events, have inflicted considerable damage on social, economic, human safety, ecosystem stability, and other aspects (Bador & Alexander, 2022; Barton *et al.*, 2022; Li *et al.*, 2022; Ning *et al.*, 2021; Patricola *et al.*, 2022; Prein & Mearns, 2021; Xu, 2020). Therefore, a comprehensive investigation of rainstorm events has become a crucial component in quantitatively assessing global and regional disasters and environmental risks.

China's expansive territory lies within the East Asian monsoon belt, making it susceptible to seasonal monsoon impacts. This susceptibility is evident in the prevalence of heavy rainfall events across the country, including pre-flood season rainstorms in southern China (April–May), the rainstorms caused by the plum rain (Mei-yu) front in the Jianghuai River Basin (June–July), the rainstorms in northern China (July–August), and others. Among these, the Mei-yu front rainstorm, as one of the typical disastrous weather patterns in China, plays a substantial role in shaping summer precipitation across the mid-latitude region of East Asia. Consequently, this phenomenon has garnered considerable attention from scholars (Chen *et al.*, 2022; Ding *et al.*, 2020; Ma *et al.*, 2023; Yu & Zhai, 2022).

Atmospheric rivers (ARs) are characterized as narrow, high-intensity channels of water vapor transport within the troposphere. They extend from the tropical ocean surface and subtropical regions to mid-latitude areas (Liang & Yong, 2021; Wang *et al.*, 2021; Zhu & Newell, 1994, 1998). According to the *Glossary of Meteorology*, an AR is defined as "a long, narrow, and transient corridor of strong horizontal water vapor transport that is typically associated with a low-level jet stream ahead of the cold front of an extratropical cyclone" (American Meteorological Society, 2017).

ARs often appear in warm conveyor belts preceding the cold front of an extratropical cyclone (Guo *et al.*, 2020). They are typically elongated and narrow, with lengths several times greater than their width (Dettinger, 2011; Ralph *et al.*, 2004). Serving as an important conveyor belt between ocean evaporation and continental precipitation, ARs transport a large amount of water vapor from the equatorial to polar regions, establishing an important pathway for water vapor transport in the atmospheric circulation (Zhang *et al.*, 2019). Therefore, ARs exhibit a close relationship with precipitation. Their impact extends to heavy

rainfall events, hurricanes, and other calamities, posing significant threats to natural ecosystems and human existence, and consequently influencing regional ecology and socioeconomic growth (Guo *et al.*, 2020; Lamjiri *et al.*, 2017; Liang & Yong, 2021; Mahoney *et al.*, 2016; Ralph *et al.*, 2020). Simultaneously, ARs deliver water vapor to arid regions, playing an important role in maintaining the water, momentum and energy equilibrium on Earth (Dettinger, 2016). This dynamic role is of profound significance for the planet's global hydrological cycle.

ARs exert a pivotal influence on both global and regional hydrological cycles, with earlier investigations primarily focusing on the west coast of North America and Europe. Guan and Waliser (2015) proposed an objective detection method for ARs on a global scale based on the characteristics of vertically integrated horizontal water vapor transport (IVT). Lamjiri *et al.* (2017) employed IVT to identify ARs and evaluated their impact on extreme precipitation along the west coast of the United States, confirming ARs as the main factors contributing to rainstorms in this region. These AR-induced rainstorms often exhibit prolonged durations and heightened rainfall intensities compared to other types of rainstorms (Guan *et al.*, 2018; Lamjiri *et al.*, 2017; Moore *et al.*, 2015; Waliser & Guan, 2017).

In recent years, scholars have observed a surge in AR activity across East Asia (Kim *et al.*, 2021; Liang *et al.*, 2023; Liang & Yong, 2021; Wang *et al.*, 2021). During the summer season, the westward movement of the Western Pacific Subtropical High steers ARs from the North Pacific to East Asia, affecting regions such as eastern China, Korea, and Japan. Referring to Guan's method, Kim *et al.* (2021) analyzed AR-related precipitation patterns in East Asia and identified a substantial increase in daily precipitation linked to ARs, particularly in heavy and extreme precipitation events. Liang *et al.* (2023) studied the long-term AR trends in East Asia from 1951 to 2015, establishing a strong correlation between ARs and extreme precipitation. It has been reported that the existence of ARs is an important influencing factor for the climate model of "dry in the north and humid in the south" in East Asia (Greve *et al.*, 2014; Liang *et al.*, 2023; Liu *et al.*, 2015; Ye *et al.*, 2013; Zhang *et al.*, 2020). Utilizing the 2020 Mei-yu season as a case study, Wang *et al.* (2021) investigated the association between ARs and Mei-yu rainfall in China, highlighting the critical role of ARs within the Mei-yu system and their pivotal influence on Mei-yu rainfall.

As rainstorm occurrences dependent on sufficient water vapor sources, ARs, functioning as robust water vapor conveyor belts, consistently supply moisture. Given that Mei-yu rainfall significantly impacts the Jianghuai River Basin, quantifying the influence of ARs on Mei-yu

rainstorms and associated disasters holds great importance for future investigations. This study focuses on a representative extreme rainstorm during the 2022 Mei-yu period, conducting a comprehensive analysis of water vapor conditions throughout the period while highlighting the quantitative impact of ARs on Mei-yu precipitation. The subsequent sections outline the study's structure and content. The second section presents the data and methods employed, including AR identification, alongside the statistical techniques used to evaluate precipitation intensity variations across different scenarios. The third section describes the occurrence and development of the Mei-yu rainstorm, the water vapor trajectories, and the difference between the precipitation intensity affected by ARs and that not affected by ARs. Finally, the last section provides conclusions and discussions.

2 | DATA AND METHODS

2.1 | Data

2.1.1 | Observed precipitation data

To conduct a comprehensive analysis of precipitation associated with individual rainstorms influenced by ARs over the Jianghuai River Basin (28–34° N, 110–122° E) in June 2022, hourly precipitation data from 1200 UTC to 2400 UTC on June 27, 2022 at 13,852 rainfall stations were used. Additionally, for a more extensive investigation into the precipitation patterns over the Jianghuai River Basin during the Mei-yu period, daily precipitation data from these rainfall stations covering the period from 2017 to 2022 were also used. Daily precipitation data less than 0.1 mm were excluded from the analysis. The geographical distribution of these rainfall stations is depicted in Figure 1a. To enhance spatial accuracy, we employed the kriging interpolation method to interpolate the data, achieving a horizontal resolution of $0.25° \times 0.25°$. Both datasets were provided by Anhui Institute of Meteorology Sciences.
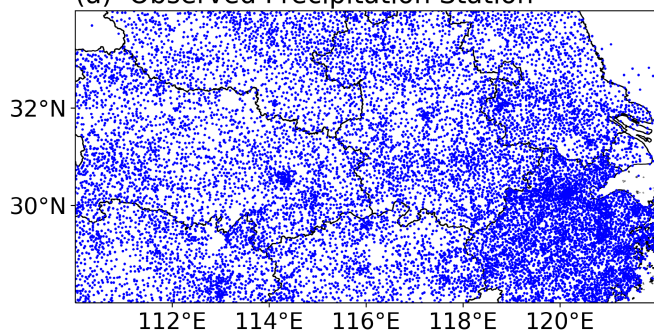
2.1.2 | Reanalysis data

The meteorological variables over the Jianghuai River Basin during the Mei-yu period of 2022 have been extracted from the ERA5 reanalysis dataset provided by the European Center for Medium-Range Weather Forecasts (ECMWF). These variables include specific humidity (q), zonal and meridional components of wind (u and v) and vertical velocity (ω) at 27 altitudinal levels from 1000 to 100 hPa. The spatial resolution of this dataset is $0.25° \times 0.25°$, accompanied by a temporal resolution of one hour.

2.1.3 | Radiosonde data

Radiosonde data obtained from the University of Wyoming contribute to our understanding of the meteorological conditions within the Jianghuai River Basin during the Mei-yu period of 2022. This dataset comprises essential variables, including temperature, humidity, wind direction, and wind speed, with a temporal resolution of twice a day (0000 and 1200 UTC). This dataset has a total of 13 stations strategically distributed across the Jianghuai River Basin to ensure even spatial coverage (see Figure 1b). The station name, station number, longitude and latitude of each station in Figure 1b are listed in Table 1.

2.1.4 | Global data assimilation system data

The global data assimilation system (GDAS) dataset is employed in the Hybrid Single-Particle Lagrangian Integrated Trajectory (HYSPLIT) model, developed by the Air Resources Laboratory (ARL) of the National Oceanic and Atmospheric Administration (NOAA). This dataset operates with a temporal resolution of 6 hours and a horizontal resolution of $2.5° \times 2.5°$, including variables such as temperature, specific humidity, zonal and meridional components of wind, etc. Spanning from January 2005 to
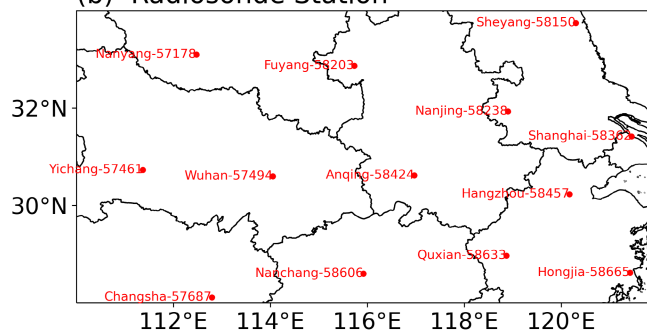
FIGURE 1 Map showing the locations of observed hourly precipitation stations (a) and radiosonde stations (b). [Colour figure can be viewed at wileyonlinelibrary.com]

TABLE 1 The station name, station number, longitude and latitude of each station in Figure 1b.

Station name	Station number	Latitude (° N)	Longitude (° E)
Shanghai	58,362	31.42	121.45
Anqing	58,424	30.62	116.97
Hongjia	58,665	28.62	121.42
Yichang	57,461	30.73	111.37
Wuhan	57,494	30.6	114.05
Hangzhou	58,457	30.23	120.17
Quxian	58,633	28.97	118.87
Nanchang	58,606	28.6	115.92
Changsha	57,687	28.11	112.79
Sheyang	58,150	33.75	120.3
Nanjing	58,238	31.93	118.9
Fuyang	58,203	32.87	115.73
Nanyang	57,178	33.10	112.48

the present, the dataset archives records for five weeks each month. In this study, the HYSPLIT model is used to trace the trajectory of water vapor within rainstorms.

2.2 | Methods

2.2.1 | AR detection

The explicit identification of ARs constitutes a pivotal phase in the investigation of these phenomena. At present, the widely accepted method involves utilizing IVT as one of the key diagnostic criteria for ARs. In this study, we adopted the AR identification methodologies outlined by Guan and Waliser (2015), Wang *et al.* (2021) and Liang and Yong (2021). By employing meteorological grid data (ERA5), we identified ARs influencing the Jianghuai River Basin through the following steps:

Firstly, we calculated the hourly IVT over East Asia and the western Pacific region (10–60° N, 100–180° E) using the following equation:

$$\text{IVT} = \sqrt{\left(\frac{1}{g}\int_{P_0}^{P_{\text{top}}} qudp\right)^2 + \left(\frac{1}{g}\int_{P_0}^{P_{\text{top}}} qvdp\right)^2} \quad (1)$$

where q represents specific humidity in kg·kg^{-1}, u and v represent zonal and meridional components of wind in m·s^{-1}, P_{top} is the pressure at the top of the atmosphere (100 hPa) and P_0 is the pressure at sea level (1000 hPa), and g is the acceleration of gravity in m·s^{-2}.

Subsequently, all grids with an IVT of 500 kg·m^{-1}·s^{-1} or larger are selected, and contiguous areas formed by these grids are discerned and isolated. Then, the area, axis lengths, and equivalent width of each distinct continuous area are calculated. It is noted that the equivalent width is defined as the ratio of the area value to the axis length.

Lastly, contiguous areas with an axis length greater than 2000 km and an equivalent width less than 750 km are identified as ARs. Within the scope of this study, our primary objective is to assess the impact of ARs on the Jianghuai River Basin. To achieve this, we establish two criteria: firstly, ARs must cover at least 10% of the Jianghuai River Basin; and secondly, there should be a minimum IVT value of 900 kg·m^{-1}·s^{-1} within the region. The fulfillment of both criteria indicates that ARs are considered to have an impact on the Jianghuai River Basin.

2.2.2 | Precipitation statistics

Grid-based analysis
To initiate our analysis, we employ the previously outlined AR identification methodology to identify the hourly occurrences of ARs influencing the Jianghuai River Basin during the 2022 Mei-yu period. If such AR events occur at least once within a specific day, that day is categorized as an "AR day"; otherwise, it is classified as a "non-AR day." Subsequently, we calculate the daily average IVT within the Jianghuai River Basin. Moreover, we categorize the daily precipitation grids into two groups based on their IVT values: those with IVT greater than 500 kg·m^{-1}·s^{-1} and those with IVT less than 500 kg·m^{-1}·s^{-1}.

Subsequently, we classify the daily precipitation grids into three distinct categories during the 2022 Mei-yu period (23 days). Class A includes grids corresponding

to AR days with IVT greater than $500 \, \text{kg} \cdot \text{m}^{-1} \cdot \text{s}^{-1}$, signifying regions unequivocally influenced by ARs. Class B comprises grids with IVT less than $500 \, \text{kg} \cdot \text{m}^{-1} \cdot \text{s}^{-1}$, generally positioned near AR-affected areas in the Jianghuai River Basin but experiencing less pronounced AR impacts. It is worth noting that, in Class B, grids are considered solely based on IVT values, irrespective of whether they fall on AR days or non-AR days. Class C includes grids situated within non-AR days but with IVT greater than $500 \, \text{kg} \cdot \text{m}^{-1} \cdot \text{s}^{-1}$, indicating areas predominantly unaffected by ARs. Therefore, for any specific grid on each day, it will be either Class A or Class B on AR days and Class B or Class C on non-AR days.

Following this, we aggregate the daily precipitation for each grid based on the previously mentioned classification conditions. This allows us to calculate the cumulative precipitation for each grid within each category. Subsequently, we divide the cumulative value by the number of days covered by each respective grid, resulting in the precipitation intensity for each grid within these three classification conditions.

Day-based analysis

Applying the procedure detailed in Section 2.2.2.1, we categorize the Mei-yu days of 2022 into two distinct groups: AR days and non-AR days. Subsequently, we aggregate the daily precipitation observed during AR days and non-AR days, respectively, within the Jianghuai River Basin. This summation provides the total precipitation for each category. To ascertain the precipitation intensity for both AR and non-AR days, we calculate the quotient by dividing the total precipitation by the respective number of AR days and non-AR days.

3 | RESULTS

3.1 | AR-related precipitation

3.1.1 | Precipitation pattern

Figure 2 illustrates the spatial distribution of total precipitation over a 12-hour period within the Jianghuai River Basin, from 1200 to 2400 UTC on June 27, 2022. During this 12-hour precipitation event, most areas experience precipitation levels ranging from 0 to 25 mm. Notably, a concentrated area of heavy precipitation emerges in the junction area of Hubei, Henan, and Anhui provinces (Figure 2). Within this region, a rainstorm belt prevails, generally oriented from southwest to northeast, with precipitation values generally exceeding 50 mm and in some areas surpassing 100 mm. In select regions, accumulated precipitation even reaches more than 250 mm. The
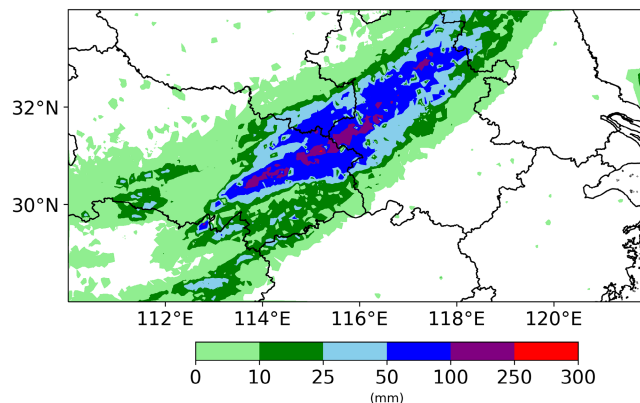
FIGURE 2 Accumulated precipitation over the Jianghuai area from 1200 to 2400 UTC on June 27, 2022. The accumulated precipitation values were derived by aggregating and interpolating the measured hourly precipitation data using the kriging interpolation method.

Dakuaidi station (31.09° N, 115.22° E) located in Huanggang City, Hubei Province, recorded the highest hourly precipitation during this event at 115.1 mm. Additionally, the elevation of this station is 721 m, higher than other stations, indicating the significant potential impact of station elevation and local topography on precipitation patterns.

3.1.2 | Vertical distribution of atmospheric circulation background

Given the limited number of sounding stations, we selected the Anqing station depicted in Figure 3, which was located closest to the rainstorm center, for analyzing the vertical distribution of the atmospheric background. Throughout this 12-hour rainfall event, a significant decrease in temperature is observed at altitudes below 700 hPa (Figure 3a). Notably, the horizontal wind speed remains relatively high throughout the precipitation period, spanning from 1000 to 300 hPa, with peaks exceeding $23 \, \text{m} \cdot \text{s}^{-1}$ (Figure 3b). The highest wind speed occurs at 0000 UTC on June 28, coinciding with the cessation of the rainstorm. Furthermore, during the precipitation event, there is an increase in specific humidity within the range of 500–850 hPa, while a decrease is observed within the layer of 850–1000 hPa (Figure 3c).

3.1.3 | Water vapor trajectories

Dakuaidi station, characterized by the highest hourly precipitation, is chosen as the representative of the rainstorm center to investigate the trajectory of water vapor within rainstorms. We establish the simulated initial heights at altitudes of 1500 m (825 hPa), 3000 m (683 hPa), and
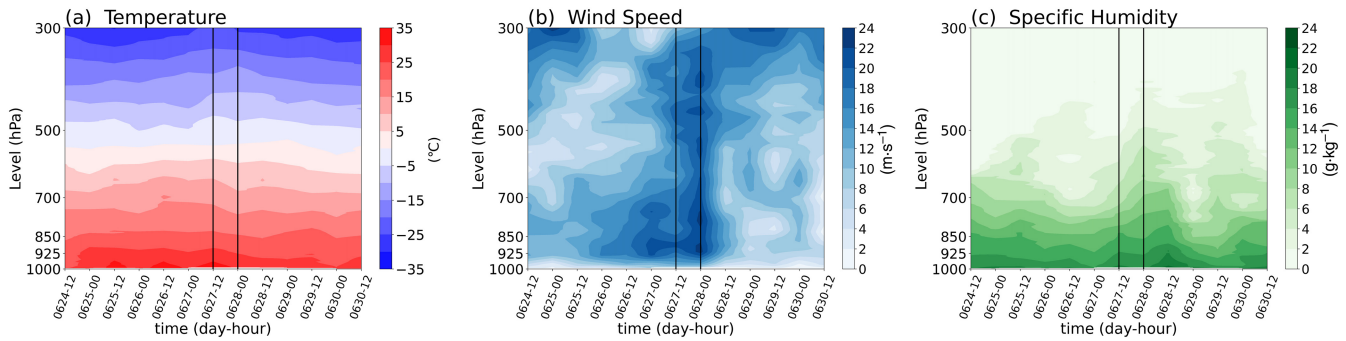
FIGURE 3 Vertical variations of (a) temperature, (b) wind speed and (c) specific humidity at Anqing Station from 1200 UTC on June 24 to 1200 UTC on June 30, 2022. The vertical lines denote the start and end times of intense precipitation.
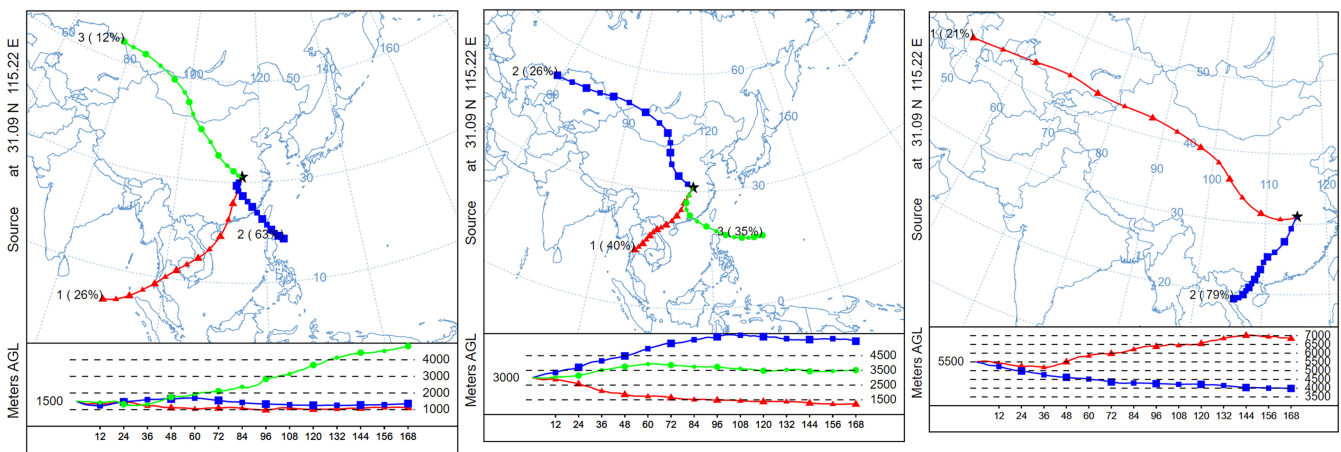
FIGURE 4 Backward water vapor transport path simulation for 168 hours at Dakuaidi Station. The simulation is conducted at three different initial altitudes: left panel – 1500 m (825 hPa), middle panel – 3000 m (683 hPa), and right panel – 5500 m (502 hPa), commencing at 2100 UTC on June 27, 2022. The accompanying diagram illustrates the height (AGL) of the air mass at different time points.

5500 m (502 hPa). The simulation is initiated from 2100 UTC on June 27, 2022, and extends over 168 hours backward by tracing three-dimensional pathways of water vapor. Subsequently, positions and heights above ground level (AGL) are recorded at six-hour intervals. Finally, the obtained backward trajectories are subjected to clustering analysis (Figure 4).

It is observed that the water vapor paths at 1500 m exhibit minimal vertical movement. However, a pronounced upward motion is evident in the water vapor trajectory originating from the southwest direction of the Bay of Bengal at 3000 m. At 5500 m, notable uplift is observed in the southwest water vapor path, while both southwest- and northwest-bound water vapor paths exhibit ascent around 36 hours before reaching the rainfall area. Drawing from the insights presented in Section 3.1.2, we deduce that the rainstorm occurred within the altitude range of 3000–5500 m.

3.1.4 | AR analysis

A distinct AR phenomenon is evident in southeast China throughout this 12-hour rainstorm. Figure 5 illustrates precipitation patterns alongside the corresponding IVT and the product of IVT and vertical velocity (ω) at three selected times during the event. The entirety of the rainfall belt and the IVT show a consistent southwest to northeast trend. In the central region of the rainstorm, IVT values remain significant at all times, consistently exceeding 900 kg·m^{-1}·s^{-1}, and even reaching 1100 kg·m^{-1}·s^{-1} at certain moments (Figure 5b,e,h). It becomes apparent that the direction of the AR aligns with the development of the rainfall belt, moving southeastward during this rainstorm event. Remarkably, both the peak area of IVT (Figure 5b,e,h) and the center of the rainstorm (Figure 5a,d,g) exhibit northeastward movement in tandem with the progression of time.
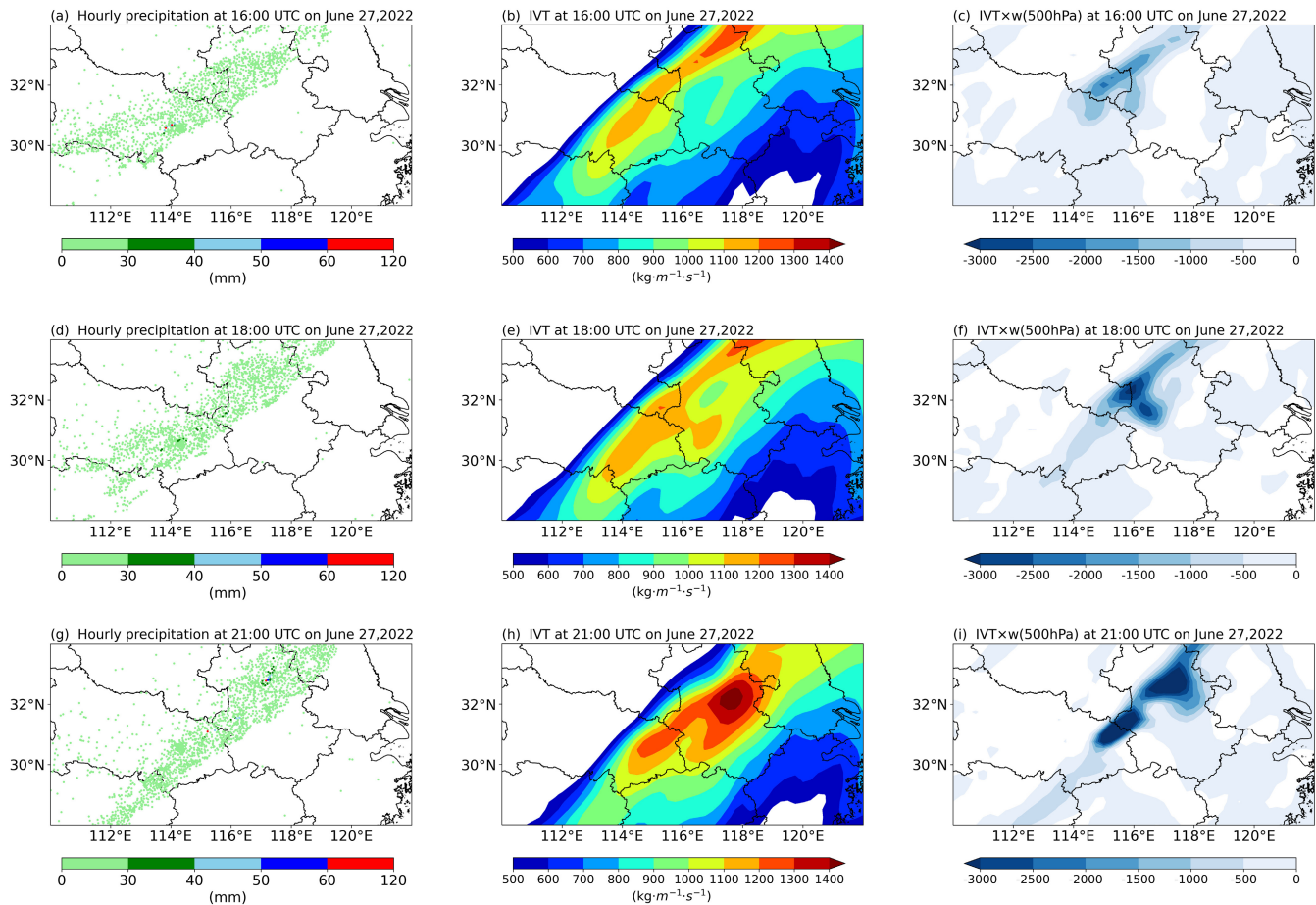
FIGURE 5 The left column is the hourly precipitation, the middle column is the distribution of atmospheric rivers (ARs), and the right column is the result of multiplying the integrated vapor transport (IVT) by the negative vertical velocity (representing upward motion) at 500 hPa. The time of the first row is 1600 UTC on June 27, 2022, the second row is 1800 UTC on June 27, 2022, and the third row is 2100 UTC on June 27, 2022.

According to IVT results, the AR covers a considerable geographical extent; however, intense precipitation is concentrated in specific regions. We speculate that this concentrations may be linked to dynamic atmospheric uplift. It is well-known that the genesis of a heavy rainstorm, aside from a continuous supply of atmospheric moisture, requires robust and sustained upward motion.

The negative value of vertical velocity represents ascending motion, which, when multiplied by the IVT values, helps us to assess the alignment between these two key essentials of rainfall and the observed precipitation distribution. Notably, at the upper level (500 hPa), the maximum negative vertical velocity demonstrates a pronounced southwest–northeast trend (Figure 5c,f,i). The peak vertical velocity value closely corresponds to both the extreme values of the rainstorm (Figure 5a,d,g) and the peak IVT values (Figure 5b,e,h). In contrast, this alignment is less distinct at lower levels (not shown). Therefore, we infer that the primary precipitation zone of this 12-hour rainstorm is at the upper levels, confirming our

earlier analytical findings. In general, substantial precipitation tends to occur when there is a substantial IVT value coupled with vigorous upward motion.

3.2 | Grid-based analysis

To quantify the AR influence over the Jianghuai River Basin on the Mei-yu period in 2022, we employed both grid-based and day-based methods to assess the differences between AR-related precipitation and non-AR-related heavy rainfall during this time frame.

The Mei-yu period in 2022 started on June 19th and ended on July 11th, spanning a duration of 23 days. According to grid-based analysis, 11 of these days are designated as "AR days," while the remaining 12 days fall into the category of "non-AR days." Moreover, each grid is divided into three categories: Class A (grids with an IVT value greater than 500 kg·m^{-1}·s^{-1} on AR days), Class B (grids with an IVT value less than 500 kg·m^{-1}·s^{-1})
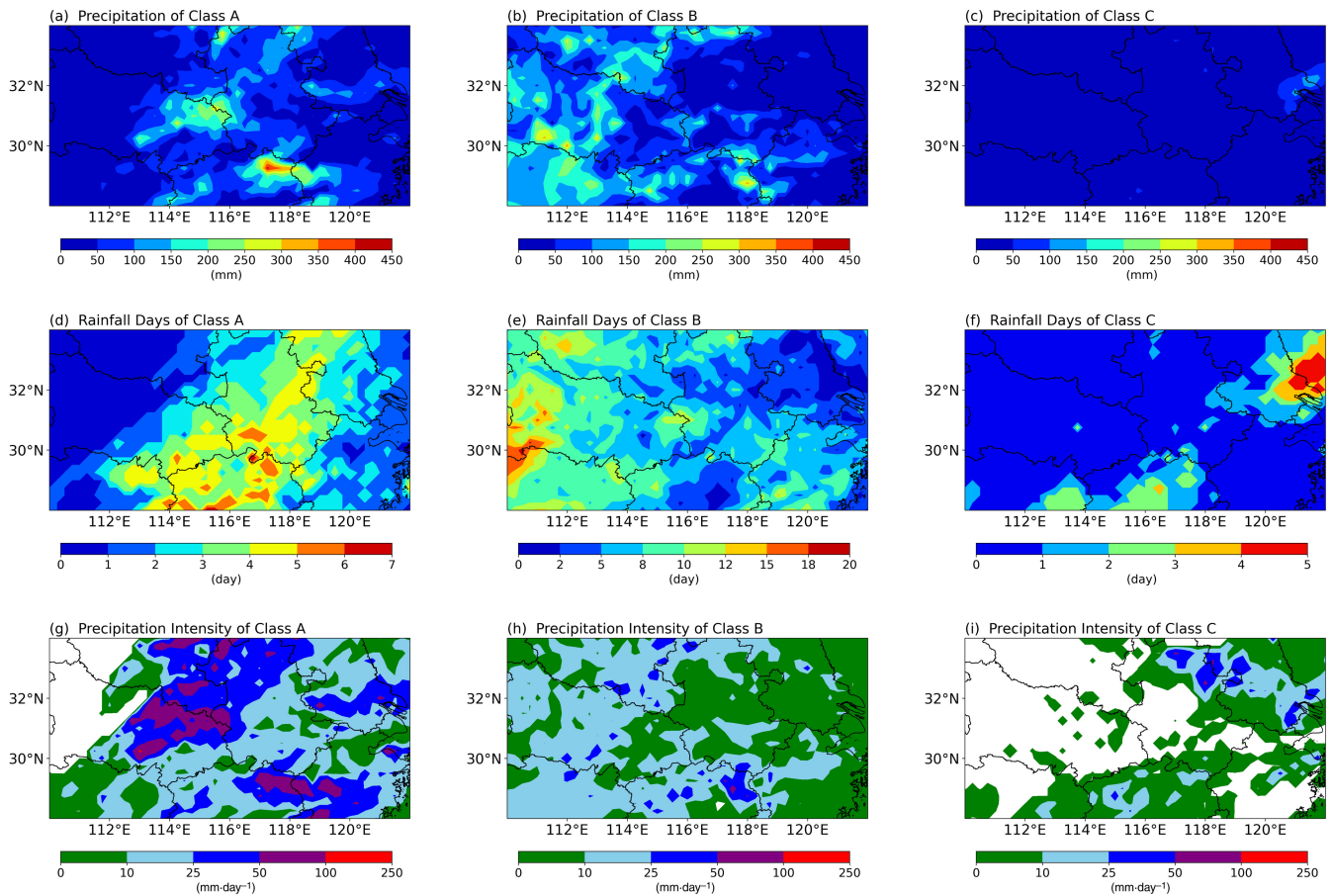
FIGURE 6   Results of grid-based analysis. The first row is the cumulative precipitation, the second row is the number of days with rainfall, and the third row is the precipitation intensity. The left column corresponds to Class A grids, the middle column to Class B grids, and the right column to Class C grids.

and Class C (grids with an IVT value greater than 500 kg·m^{-1}·s^{-1} on non-AR days).

Figure 6 presents the cumulative precipitation, the number of rainfall days, and the precipitation intensity for each grid across three distinct categories. For Class A grids, notably affected by ARs, the highest cumulative precipitation values are concentrated in the central part of the Jianghuai River Basin, a region exhibiting pronounced AR activity. The central areas witness individual instances of precipitation reaching up to 200 mm, with maximum values even exceeding 400 mm (Figure 6a). Despite their substantial cumulative precipitation, Class A grids experience fewer precipitation days, with a maximum of seven days (Figure 6d). This combination of larger precipitation and fewer rainfall days results in stronger precipitation intensity (Figure 6g).

Across the Jianghuai River Basin, precipitation intensity in Class A grids during the Mei-yu period generally exceeds 10 mm·day^{-1}, ranging from 25 to 50 mm·day^{-1} in most regions, meeting the criteria for heavy rain. For some grids, the range extends from 50 to 100 mm·day^{-1}, meeting

the threshold for a rainstorm. In a few select regions, the maximum value even surpasses 100 mm·day^{-1}, reaching 107 mm·day^{-1} and attaining the classification of a heavy rainstorm.

It is worth noting that Class B grids encompass all instances where IVT values are less than 500 kg·m^{-1}·s^{-1}, regardless of whether AR events occurred on that particular day. According to Figure 6, Class B grids are still impacted by ARs. Even if AR events are present, Class B grids are predominantly positioned in proximity to the ARs without direct influence. Precipitation in Class B grids is mainly concentrated in the western Jianghuai River Basin. In most regions, the cumulative precipitation of Class B remains below 150 mm, with isolated areas ranging from 150 to 250 mm, and a few grids reaching 300 mm (Figure 6b). Despite Class B grids having IVT values below 500 kg·m^{-1}·s^{-1}, their locations may be situated in areas where ARs weaken or dissipate. Consequently, they might indirectly experience the influence of ARs, leading to the continued occurrence of precipitation. This influence potentially results in an increase in the number of rainfall

days for Class B, with these grids experiencing numerous days of rainfall, generally exceeding eight days and reaching a maximum of over 18 days (Figure 6e). The extensive rainfall duration contributes to reduced precipitation intensity (Figure 6h).

Across most of the Jianghuai River Basin, precipitation intensity of Class B grids ranges from 0 to 25 mm·day^{-1}, with some areas reaching 25–50 mm·day^{-1}, just meeting the criteria for heavy rain. Only in individual areas can the precipitation intensity reach 50–100 mm·day^{-1}, meeting the threshold for a rainstorm.

Class C girds demonstrate minimal AR influence, typically occurring during periods without AR presence or during the decay phase of AR events that do not impact the Jianghuai River Basin. Cumulative precipitation for Class C grids is basically below 50 mm, accompanied by fewer than five days, leading to relatively low precipitation intensity (Figure 6c–i). Precipitation intensity across these grids generally ranges from 0 to 10 mm·day^{-1}, meeting the classification of light rain. In select regions, it reaches 10–50 mm·day^{-1}, satisfying the criteria for moderate to heavy rain.

We also investigated the probability distribution of precipitation intensity for the three classes of grids (not shown). On AR days and for the grids with IVT values larger than 500 kg·m^{-1}·s^{-1} (Class A), the median, 75th percentile and 95th percentile of the precipitation

intensity are 14.32 mm·day^{-1}, 30.03 mm·day^{-1}, and 57.89 mm·day^{-1}, respectively. For Class B, these values are 9.58 mm·day^{-1}, 15.18 mm·day^{-1}, and 24.69 mm·day^{-1}. On non-AR days and for the girds with IVT values larger than 500 kg·m^{-1}·s^{-1} (Class C), half of the area has no rain and the 75th percentile precipitation intensity of Class C grids is only 3.36 mm·day^{-1}. This indicates that Class A, strongly affected by ARs, exhibits higher median and extreme precipitation values compared to Class B, which is consistent with the previous reported results (Kim et al., 2021; Wang et al., 2021). Class C, with minimal AR influence, generally experiences lower precipitation intensities.

When dividing the precipitation intensity in Class A by the precipitation intensity in Class B and Class C (Figure 7), it becomes evident that the precipitation intensity of Class A is generally 4–20 times that of Class B. For certain grids, this value exceeds 30. Regarding Class C grids, the ratio is larger than 24 in many areas. This highlights the significant role of ARs in enhancing the intensity of heavy rainfall events.

In terms of the climatology, the study explored the precipitation intensity ratios among three grid classes during Mei-yu seasons over the period 2017–2022 (Figure 8). For each grid, the ratio of Class A to Class B is mostly 2–8 across the study region, with the maximum values occurring in the northwest part (Figure 8a). Generally, the ratio of Class
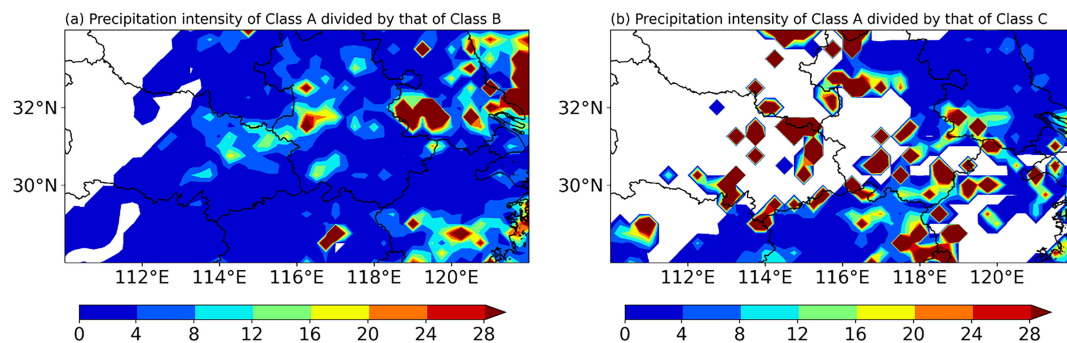
FIGURE 7 Comparison of precipitation intensity ratios between (a) Class A and Class B grids, and (b) Class A and Class C grids.
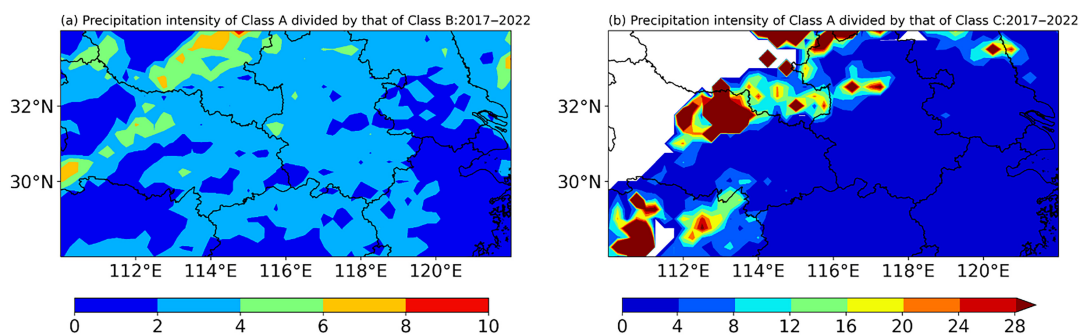
FIGURE 8 Similar to Figure 7, but for the period of 2017–2022.
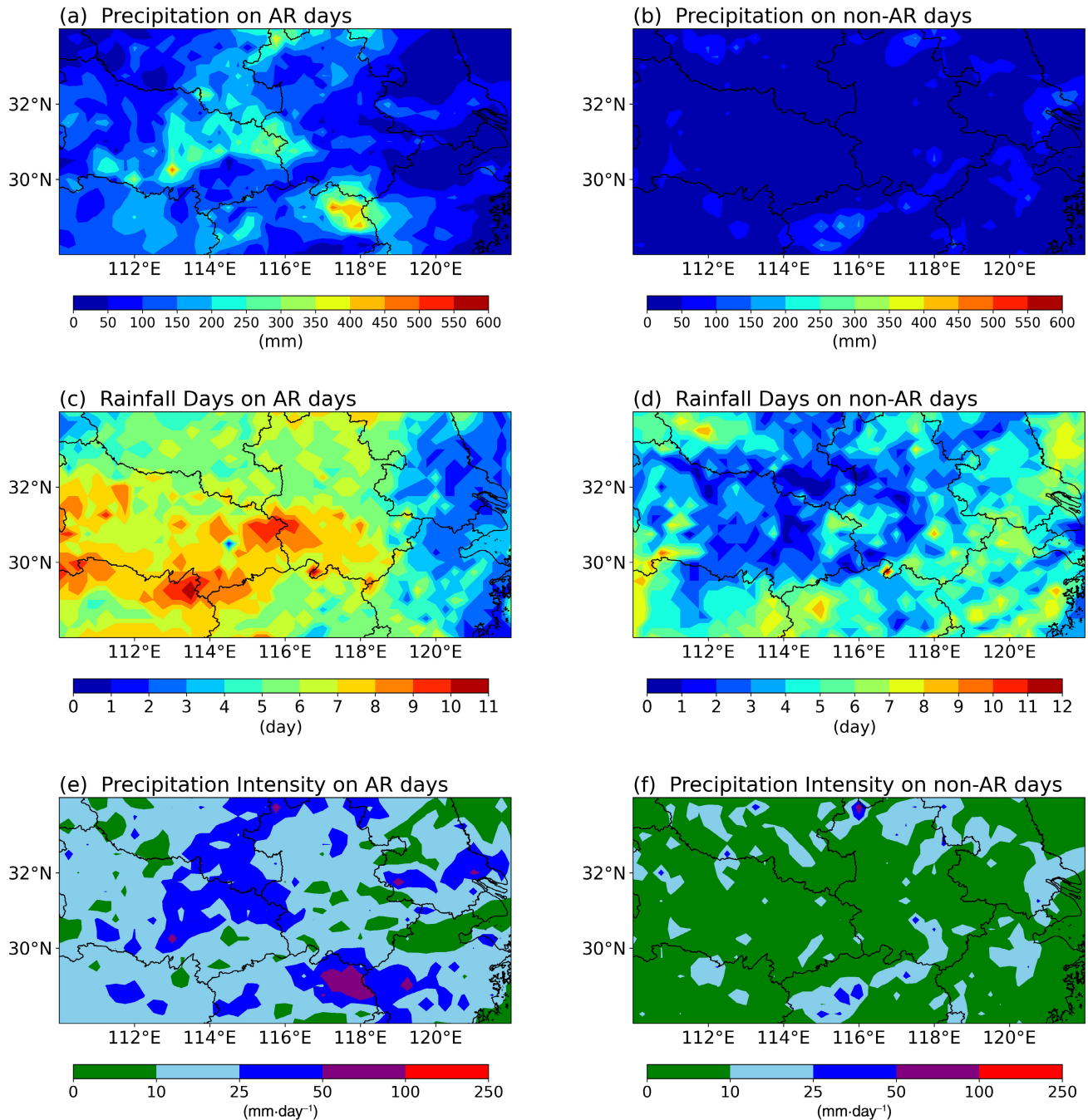
FIGURE 9 Results of day-based analysis. The first row represents total precipitation, the second row represents the number of days with rainfall and the third row represents precipitation intensity. The left column corresponds to atmospheric river (AR) days and the right column corresponds to non-AR days.

A to Class C is larger than those of Class B, and areas with the larger ratio are also located in the northwest part of the region (Figure 8b), with much greater values (8–30 times or even higher).

We speculate that, even though Class B grids are distant from ARs, the influence of ARs may indirectly lead to a continued occurrence of precipitation in these regions. This may result in the relatively smaller ratio of Class A to Class B in the longer period unaffected by ARs.

3.3 | Day-based analysis

In this section, the Mei-yu period is segmented into AR days and non-AR days, and their respective precipitation intensities are calculated. As shown in Figure 9, the total precipitation on AR days (Figure 9a) significantly exceeds that on non-AR days (Figure 9b). The distribution of total precipitation on AR days is similar to the findings in Figure 6a, with high values concentrated

in the convergence area of Hubei, Henan, and Anhui provinces, as well as in the northeastern part of Jiangxi province, where maximum values exceed 400 mm. Conversely, precipitation on non-AR days generally remains below 100 mm. The number of AR days varies from four to 10 across the majority of the study region (Figure 9c), whereas the count of non-AR days spans from one to eight (Figure 9d).

Furthermore, precipitation intensity on AR days markedly exceeds that on non-AR days. Specifically, across most of the Jianghuai River Basin, precipitation intensity ranges between 0 and 25 mm·day^{-1} on AR days, meeting the criteria for light to moderate rain. In central regions, it escalates to 25–50 mm·day^{-1}, indicative of heavy rain. In a select few regions, the range even extends from 50 to 100 mm·day^{-1}, meeting the threshold for a rainstorm (Figure 9e). In contrast, precipitation intensity on non-AR days usually falls between 0 and 25 mm·day^{-1}, reflecting light rain and moderate rain (Figure 9f). Only in individual areas, it can meet the criteria for heavy rain.

Dividing the precipitation intensity of each grid on AR days by the precipitation intensity on non-AR days yields the distribution of the ratio (Figure 10). Figure 10a presents the results for the Mei-yu period in 2022, and Figure 10b shows the results for the period 2017–2022. In the 2022 case, the precipitation intensity on AR days can be as high as 30 times that on non-AR days, with ratios larger than 8 observed in many areas. Regarding the six-year averaged results (Figure 10b), precipitation intensity on AR days is generally 2–5 times that of non-AR days. This wide variation underscores the substantial influence of ARs on precipitation intensity.

It is important to acknowledge that, on average, this methodology might attenuate the intensity of rainstorms in individual areas, potentially resulting in calculated values for rainstorm intensity that are smaller than the actual figures. Nevertheless, even with this consideration, it is evident that AR-related rainstorm intensities are 2–5 times

higher than those associated with non-AR conditions, if not significantly more.

3.4 | Comparisons between grid-based and day-based analysis

Grid-based analysis primarily focuses on individual geographical grid points, categorizing the study area into different grid classes (Class A, B, C). By comparing these different grid classes, it reveals the impact of ARs on precipitation characteristics in different contexts.

In comparisons among these three classes, a grid-based analysis perspective provides valuable insights. The results of Class A grids underscore the significant role of ARs in intensifying heavy rainfall events. In contrast, Class B grids exhibit a trend less associated with ARs, displaying IVT values generally below 500 kg·m^{-1}·s^{-1}. However, Class B grids are often situated in areas adjacent to ARs, where the influence of ARs may indirectly lead to continued occurrence of precipitation. This can result in a higher number of days with rainfall, albeit with decreased rainfall intensity. For Class C grids, which are essentially unaffected by ARs, they typically occur during periods without ARs or during the dissipating phase of ARs that do not impact the Jianghuai River Basin. Consequently, precipitation amounts, the number of rainfall days, and rainfall intensity are relatively lower.

Day-based analysis divides time into AR days and non-AR days, then calculates their respective precipitation intensities. By comparing the precipitation on AR days and non-AR days, it is concluded that during the Mei-yu period, total precipitation on AR days is significantly higher than on non-AR days. According to the six-year averaged precipitation intensity ratio results obtained through day-based analysis (Figure 10b), the ratio is generally smaller than that of grid-based analysis (Figure 8). This discrepancy is attributed to the fact
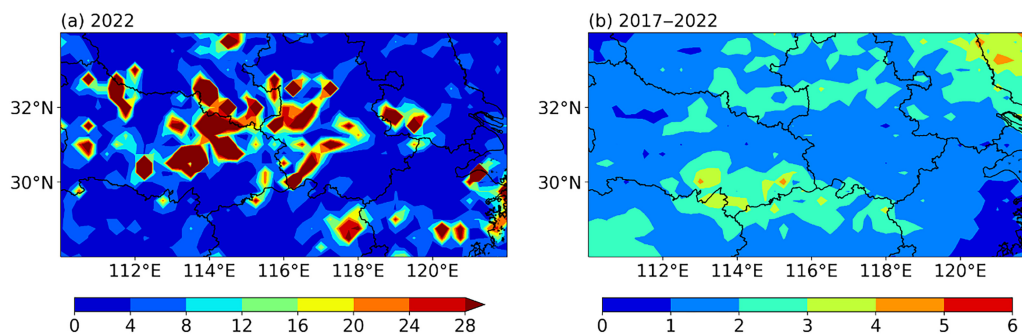
FIGURE 10 The ratio of precipitation intensity on atmospheric river (AR) days to non-AR days for (a) 2022 and (b) the period of 2017–2022.

that, in day-based analysis, ARs may occur in different regions on different days, attenuating the intensity of rainstorms on a long-term averaged basis across the study region.

Grid-based analysis emphasizes detailed differences on various geographical points within the region, providing an in-depth understanding of the degree of the impact of ARs at different locations. Day-based analysis emphasizes the overall precipitation contrast between AR and non-AR days throughout the Mei-yu period, offering a more macroscopic perspective. The combination of both analyses allows a comprehensive understanding of AR influence, blending detailed spatial variations (grid-based) with broader temporal trends (day-based).

4 | DISCUSSIONS AND CONCLUSIONS

During the Mei-yu period in 2022, multiple rainstorm events occurred in the Jianghuai River Basin. This study began by examining the atmospheric circulation patterns, water vapor attributes, and transport trajectories associated with a specific rainstorm occurring on June 27, 2022. Subsequently, we conducted a comprehensive investigation into the differences between precipitation affected by ARs and precipitation not affected by ARs throughout the Mei-yu period in 2022. Additionally, we quantified the magnitude of ARs' impact on precipitation in the region.

The water vapor transport path during the heavy rain on June 27, 2022, showed obvious upward movement between 500 and 700 hPa. This strong upward movement provided favorable conditions for the development of the rainstorm. Between 500- and 700-hPa levels, there is a significant temperature drop in the center of the storm due to water vapor condensation. A prevailing southwest wind transported substantial moisture from the Bay of Bengal region to the Jianghuai River Basin. Concurrently, a northwest wind contributed to the southeastward movement of the rainfall belt, aligning with the process of precipitation occurrence and development.

Throughout this rainstorm event, a prominent southwest-to-northeast-oriented AR manifested within the Jianghuai River Basin. The direction of the AR was consistent with the development of the rain belt and moved southeastward. Notably, the region with the highest IVT also shifted in the same direction as the rainstorm center, both tracking northeastward.

To further analyze the influence of ARs on Mei-yu season rainfall, ERA5 data were used to determine the appearance of ARs. The 23-day Mei-yu period is divided into two distinct groups: AR days (11 days) and non-AR days (12 days). This division enables a clearer differentiation between the meteorological conditions during AR-influenced days and those during periods without ARs. Following this initial categorization, the daily precipitation data are further classified into two groups based on a threshold IVT value of $500\,\mathrm{kg\cdot m^{-1}\cdot s^{-1}}$. Subsequently, these daily precipitation grids we4re categorized into three distinct classes. This refined categorization facilitated a more granular analysis, providing valuable insights into the impact of ARs on precipitation patterns at the grid level.

The impact of ARs on precipitation exhibited significant variations across the three defined classes of grids. Class A grids, significantly influenced by ARs, received substantial precipitation in the central Jianghuai River Basin, often exceeding 400 mm, with daily intensity between 25 and $50\,\mathrm{mm\cdot day^{-1}}$, even reaching rainstorm thresholds in some areas. Class B grids, moderately affected by ARs, saw precipitation mainly in the western Jianghuai River Basin, with intensity between 0 and $30\,\mathrm{mm\cdot day^{-1}}$, occasionally reaching criteria for heavy rain but rarely rainstorm levels. Class C grids, untouched by ARs, experienced minimal precipitation. Most areas had no rain, while some observed light rain with an intensity of $0\text{–}10\,\mathrm{mm\cdot day^{-1}}$.

For each grid, the six-year averaged precipitation intensity ratio of Class A to Class B is mostly 2–8 across the study region, while the ratio of Class A to Class C is generally larger, with values ranging from eight to 30 times. It is important to note that this ratio in one year or a single case could be much larger than the six-year averaged values.

In summary, the probability of experiencing rainstorm events is notably higher for Class A grids, experiencing pronounced AR activity and substantial AR influence. Class B grids, typically situated near ARs, exhibit a moderate influence and a lower probability of rainstorms, but experience a longer durations of rainy days. Class C grids remain entirely unaffected by ARs, often occurring during periods without ARs or during the dissipating phase of ARs that do not affect the Jianghuai River Basin. This indicates that despite IVT exceeding $500\,\mathrm{kg\cdot m^{-1}\cdot s^{-1}}$, there is little chance for the region to have rainstorm events during AR-free periods or the dissipating phase of ARs.

For the day-based analysis, the Mei-yu period was divided into AR days and non-AR days to compare their precipitation intensities. It is worth noting that only a small portion (~25%) of areas experience rainstorms on AR days. This discrepancy might arise from the methodology potentially underestimating precipitation intensity in some regions, resulting in calculated values lower than the

actual figures. The six-year averaged precipitation intensity on AR days is generally 2–5 times that of non-AR days, while in specific years or single cases, the ratio could reach up to 30 times.

Both statistical methods reveal the amplifying impact of ARs on heavy precipitation events, showcasing significantly higher precipitation intensity in the presence of ARs compared to their absence. The grid-based analysis offers a detailed spatial perspective, highlighting localized areas significantly influenced by ARs. On the other hand, the day-based analysis provides a temporal view, allowing for a nuanced understanding of how ARs affect precipitation over time.

Quantitatively, the grid-based analysis indicates that precipitation intensity during AR events (Class A) is, on average, 8–30 times higher than in non-AR periods (Class C) in the western part of the study region. In contrast, the day-based analysis demonstrates an average precipitation intensity ratio of 2–5 times on AR days compared to non-AR days. These results underscore the robustness of ARs in enhancing heavy precipitation, emphasizing the necessity of considering both spatial and temporal dimensions in understanding their influence on rainfall patterns.

However, it is essential to note that the mere presence of ARs does not guarantee extreme precipitation. Indeed, ARs contribute a substantial supply of water vapor, but the occurrence of heavy rain is also influenced by factors such as the strength of vertical ascent and local topography. Generally, when these influencing factors align and are sufficiently robust, the likelihood of rainstorm events significantly increases.

DATA AVAILABILITY STATEMENT
The radiosonde data used in this study are derived from http://weather.uwyo.edu/upperair/bufrraob.shtml. ERA5 data can be accessed from the European Center for Medium-Range Weather Forecasts (https://cds.climate.copernicus.eu/cdsapp#!/dataset/reanalysis-era5-pressure-levels?tab=form). The rainfall station data used in this study are available on request from the corresponding author. The data are not publicly available due to privacy or ethical restrictions.

ORCID
Y. Zhang https://orcid.org/0000-0002-1448-0119

REFERENCES
American Meteorological Society. (2017) Atmospheric river. Glossary of Meteorology. http://glossary.ametsoc.org/wiki/Atmospheric&uscore;river

Bador, M. & Alexander, L.V. (2022) Future seasonal changes in extreme precipitation scale with changes in the mean. *Earth's Futures*, 10(12), e2022EF002979.

Barton, Y., Rivoire, P., Koh, J., Ali, S.M., Kopp, J.M. & Martius, O. (2022) On the temporal clustering of European extreme precipitation events and its relationship to persistent and transient large-scale atmospheric drivers. *Weather and Climate Extremes*, 38, 100518 https://www.sciencedirect.com/science/article/pii/S2212094722000974

Chen, C.-A., Hsu, H.-H., Liang, H.-C., Chiu, P.-G. & Tu, C.-Y. (2022) Future change in extreme precipitation in East Asian spring and Mei-yu seasons in two high-resolution AGCMs. *Weather and Climate Extremes*, 35, 100408 https://www.sciencedirect.com/science/article/pii/S2212094722000020

Dettinger, M. (2011) Climate change, atmospheric rivers, and floods in California–a multimodel analysis of storm frequency and magnitude changes. *JAWRA Journal of the American Water Resources Association*, 47(3), 514–523.

Dettinger, M. (2016) Historical and future relations between large storms and droughts in California. *San Francisco Estuary and Watershed Science*, 14(2), 1–21. https://doi.org/10.15447/sfews.2016v14iss2art1

Ding, Y., Liang, P., Liu, Y. & Zhang, Y. (2020) Multiscale variability of Meiyu and its prediction: a new review. *Journal of Geophysical Research: Atmospheres*, 125(7), e2019JD031496.

Gao, X., Zhu, Q., Yang, Z., Liu, J., Wang, H., Shao, W. et al. (2018) Temperature dependence of hourly, daily, and event-based precipitation extremes over China. *Scientific Reports*, 8(1), 17564.

Greve, P., Orlowsky, B., Mueller, B., Sheffield, J., Reichstein, M. & Seneviratne, S.I. (2014) Global assessment of trends in wetting and drying over land. *Nature Geoscience*, 7(10), 716–721.

Guan, B. & Waliser, D.E. (2015) Detection of atmospheric rivers: Evaluation and application of an algorithm for global studies. *Journal of Geophysical Research: Atmospheres*, 120(24), 12514–12535.

Guan, B., Waliser, D.E. & Ralph, F.M. (2018) An intercomparison between reanalysis and dropsonde observations of the total water vapor transport in individual atmospheric rivers. *Journal of Hydrometeorology*, 19(2), 321–337.

Guo, Y., Shinoda, T., Guan, B., Waliser, D.E. & Chang, E.K. (2020) Statistical relationship between atmospheric rivers and extratropical cyclones and anticyclones. *Journal of Climate*, 33(18), 7817–7834.

Kim, J., Moon, H., Guan, B., Waliser, D.E., Choi, J., Gu, T.-Y. et al. (2021) Precipitation characteristics related to atmospheric rivers in East Asia. *International Journal of Climatology*, 41, E2244–E2257.

Lamjiri, M.A., Dettinger, M.D., Ralph, F.M. & Guan, B. (2017) Hourly storm characteristics along the US west coast: role of atmospheric rivers in extreme precipitation. *Geophysical Research Letters*, 44(13), 7020–7028.

Li, Z., Gao, S., Chen, M., Gourley, J.J. & Hong, Y. (2022) Spatiotemporal characteristics of US floods: current status and forecast under a future warmer climate. *Earth's Futures*, 10(10), e2022EF002700.

Liang, J. & Yong, Y. (2021) Climatology of atmospheric rivers in the Asian monsoon region. *International Journal of Climatology*, 41, E801–E818.

Liang, J., Yong, Y. & Hawcroft, M.K. (2023) Long-term trends in atmospheric rivers over East Asia. *Climate Dynamics*, 60(3–4), 643–666.

Limsakul, A. & Singhruck, P. (2016) Long-term trends and variability of total and extreme precipitation in Thailand. *Atmospheric Research*, 169, 301–317.

Liu, R., Liu, S.C., Cicerone, R.J., Shiu, C.-J., Li, J., Wang, J. et al. (2015) Trends of extreme precipitation in eastern China and their possible causes. *Advances in Atmospheric Sciences*, 32, 1027–1037.

Ma, J., Wei, K., Chen, W., Wang, T. & Shi, D. (2023) The southward movement preference of large-scale persistent extreme precipitation events over the Yangtze River Valley during Mei-yu period. *Climate Dynamics*, 60(11–12), 3729–3747.

Mahoney, K., Jackson, D.L., Neiman, P., Hughes, M., Darby, L., Wick, G. et al. (2016) Understanding the role of atmospheric rivers in heavy precipitation in the southeast United States. *Monthly Weather Review*, 144(4), 1617–1632.

Moore, B.J., Mahoney, K.M., Sukovich, E.M., Cifelli, R. & Hamill, T.M. (2015) Climatology and environmental characteristics of extreme precipitation events in the southeastern United States. *Monthly Weather Review*, 143(3), 718–741.

Ning, G., Luo, M., Zhang, Q., Wang, S., Liu, Z., Yang, Y. et al. (2021) Understanding the mechanisms of summer extreme precipitation events in Xinjiang of arid Northwest China. *Journal of Geophysical Research: Atmospheres*, 126(15), e2020JD034111. Available from: https://doi.org/10.1029/2020JD034111

Patricola, C.M., Wehner, M.F., Bercos-Hickey, E., Maciel, F.V., May, C., Mak, M. et al. (2022) Future changes in extreme precipitation over the San Francisco Bay Area: dependence on atmospheric river and extratropical cyclone events. *Weather and Climate Extremes*, 36, 100440.

Prein, A.F. & Mearns, L.O. (2021) U.S. extreme precipitation weather types increased in frequency during the 20th century. *Journal of Geophysical Research: Atmospheres*, 126(7), e2020JD034287. Available from: https://doi.org/10.1029/2020JD034287

Ralph, F.M., Cannon, F., Tallapragada, V., Davis, C.A., Doyle, J.D., Pappenberger, F. et al. (2020) West coast forecast challenges and development of atmospheric river reconnaissance. *Bulletin of the American Meteorological Society*, 101(8), E1357–E1377.

Ralph, F.M., Neiman, P.J. & Wick, G.A. (2004) Satellite and CALJET aircraft observations of atmospheric rivers over the eastern North Pacific Ocean during the winter of 1997/98. *Monthly Weather Review*, 132(7), 1721–1745.

Waliser, D. & Guan, B. (2017) Extreme winds and precipitation during landfall of atmospheric rivers. *Nature Geoscience*, 10(3), 179–183.

Wang, S., Ma, X., Zhou, S., Wu, L., Wang, H., Tang, Z. et al. (2023) Extreme atmospheric rivers in a warming climate. *Nature Communications*, 14(1), 3219. Available from: https://doi.org/10.1038/s41467-023-38980-x

Wang, T., Wei, K. & Ma, J. (2021) Atmospheric rivers and mei-yu rainfall in China: a case study of summer 2020. *Advances in Atmospheric Sciences*, 38, 2137–2152.

Xu, W. (2020) Thunderstorm climatologies and their relationships to total and extreme precipitation in China. *Journal of Geophysical Research: Atmospheres*, 125(19), e2020JD033152. Available from: https://doi.org/10.1029/2020JD033152

Ye, J., Li, W., Li, L. & Zhang, F. (2013) "North drying and south wetting" summer precipitation trend over China and its potential linkage with aerosol loading. *Atmospheric Research*, 125-126, 12–19 https://www.sciencedirect.com/science/article/pii/S0169809513000446

Yu, R. & Zhai, P. (2022) An objective approach to predict the spatial property of anomalous rain-belt of Meiyu. *Weather and Climate Extremes*, 37, 100466 https://www.sciencedirect.com/science/article/pii/S2212094722000482

Zhang, Y., Ren, Y., Ren, G. & Wang, G. (2020) Precipitation trends over mainland China from 1961–2016 after removal of measurement biases. *Journal of Geophysical Research: Atmospheres*, 125(11), e2019JD031728. Available from: https://doi.org/10.1029/2019JD031728

Zhang, Z., Ralph, F.M. & Zheng, M. (2019) The relationship between extratropical cyclone strength and atmospheric river intensity and position. *Geophysical Research Letters*, 46(3), 1814–1823.

Zhu, Y. & Newell, R.E. (1994) Atmospheric rivers and bombs. *Geophysical Research Letters*, 21(18), 1999–2002.

Zhu, Y. & Newell, R.E. (1998) A proposed algorithm for moisture fluxes from atmospheric rivers. *Monthly Weather Review*, 126(3), 725–735.